Weierstraß–Institut
für Angewandte Analysis und Stochastik

im Forschungsverbund Berlin e.V.

Preprint ISSN 0946 – 8633

Numerical bifurcation analysis for multi-section semiconductor lasers

Jan Sieber[1]

submitted: 1st October 2001

[1] Weierstraß Institute
for Applied Analysis
and Stochastics
Mohrenstr. 39
D-10117 Berlin
E-Mail: sieber@wias-berlin.de

Preprint No. 683
Berlin 2001

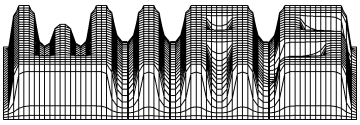

2000 *Mathematics Subject Classification.* 34C60, 78A60.

Key words and phrases. semiconductor lasers, delayed optical feedback, numerical bifurcation analysis.

Edited by
Weierstraß–Institut für Angewandte Analysis und Stochastik (WIAS)
Mohrenstraße 39
D — 10117 Berlin
Germany

Fax: + 49 30 2044975
E-Mail (X.400): c=de;a=d400-gw;p=WIAS-BERLIN;s=preprint
E-Mail (Internet): preprint@wias-berlin.de
World Wide Web: http://www.wias-berlin.de/

Abstract

We investigate the dynamics of a multi-section laser resembling a delayed feedback experiment where the length of the cavity is comparable to the length of the laser. Firstly, we reduce the traveling-wave model with gain dispersion (a hyperbolic system of partial differential equations) to a system of ordinary differential equations (ODEs) describing the semiflow on a local center manifold. Then, we analyse the dynamics of the system of ODEs using numerical continuation methods (AUTO). We explore the plane of the two parameters feedback phase and feedback strength to obtain a complete bifurcation diagram for small and moderate feedback strength. This diagram allows to understand the roots of a variety of nonlinear phenomena like, e. g., self-pulsations, excitability, hysteresis or chaos, and to locate them in the parameter plane.

1 Introduction

Semiconductor lasers subject to delayed optical feedback show a variety of nonlinear effects. Self-pulsations, excitability, coexistence of several stable regimes, and chaotic behavior have been observed both in experiments and numerical simulations [6], [11], [17], [19], [22]. Multi-section lasers allow to design and control these feedback effects and permit their application, e. g., in optical data transmission, processing and recovery [19], [31].

If mathematical modeling ought to be helpful in guiding this difficult and expensive design process, it has to meet two criteria contradicting each other. On one hand, the model should be accurate and controllable in the original physically sensible parameters. Typically, only very complex models allow for that, e. g., systems of partial differential equations (PDEs).

On the other hand, the modeling should permit insight into the nature of the nonlinear effects. This is impossible using just straight simulations, i. e., performing the experiment at the computer. Only a detailed and complete bifurcation analysis allows to find coexisting stable regimes, unstable objects which are boundaries of coexisting attracting regions, and bifurcations of higher codimension which are a common source for various nonlinear phenomena. Unfortunately, there exist numerical bifurcation tools only for low-dimensional ordinary differential equations (ODEs) [8], [15], and very restricted classes of PDEs (e. g., delay-differential equations [10]).

In this paper, we start from the traveling-wave model [3], [16], [23] which resolves the light amplitude E spatially in the longitudinal direction but treats the carrier density n as a spatially section-wise averaged quantity. For illustrative purposes, we restrict our analysis to a particular multi-section laser outline performing a classical

delayed feedback experiment (see Fig. 1). This way, the model has the structure

$$\begin{aligned} \dot{E} &= H(n)E \\ \dot{n} &= \varepsilon\left(f(n) - g(n)[E,E]\right) \end{aligned} \tag{1}$$

where the first equation is a linear hyperbolic system of PDEs for E which is nonlinearly coupled with a scalar ODE for n. This model is particularly well adapted to multi-section lasers: It is sufficiently accurate to keep track of the effects caused by the longitudinal resonator structure within the laser. On the other hand, its slow-fast structure ($\varepsilon \ll 1$) allows to derive analytically low-dimensional systems of ODEs which approximate the semiflow on a local center manifold [20], [26]. These ODEs are accessible for classical numerical bifurcation analysis tools like AUTO. This way we meet both requirements: We present reasonably complete bifurcation diagrams in the physically relevant parameters for a theoretically (and numerically [29]) justified approximation of the full PDE system (1).

One further remark on the choice of the model: another very popular model for the investigation of delayed feedback effects is the Lang-Kobayashi system [11], [14], [17], [24], [22]. It has also the structure of (1). Hence, it can be treated by the methods presented in this paper, too. However, we use the traveling-wave model as it fits better to the setting of a multi-section laser.

The outline of the paper is as follows: In the second section, we will describe the traveling-wave model in more detail and reiterate the theorem of [20] concerning the model reduction to *mode approximations*. In the third section, we perform a complete numerical bifurcation analysis of the *single-mode approximation* (a two-dimensional system of ODEs) which is a valid approximation if the feedback strength is sufficiently small. The primary bifurcation parameters are the feedback strength η and the feedback phase φ. In the third section, we derive an appropriately posed two-mode approximation (a four-dimensional system of ODEs) in the vicinity of a point where the critical eigenvalue of $H(n)$ has algebraic multiplicity two. Furthermore, we perform a numerical bifurcation analysis of this system. However, this system shows complicated dynamics such that the bifurcation analysis must remain incomplete. In the final section, we give a brief summary and an outlook to further investigations.

2 The mathematical model

2.1 The traveling-wave model with gain dispersion

Let $\psi(t) \in \mathbb{L}^2([0,L];\mathbb{C}^2)$ describe the spatially resolved complex amplitude of the optical field which is split into a forward and backward traveling wave. Let $p(t) \in \mathbb{L}^2([0,L];\mathbb{C}^2)$ be the corresponding nonlinear polarization [20], [30]. Denote the one-dimensional spatial variable by $z \in [0,L]$ (the longitudinal direction in the laser). We consider a geometric configuration as is presented in Fig. 1 where n is the spatially averaged carrier density in the first section S_1. Then, the traveling-wave model with gain dispersion [20], [30] poses an initial-boundary-value problem for ψ, p and n

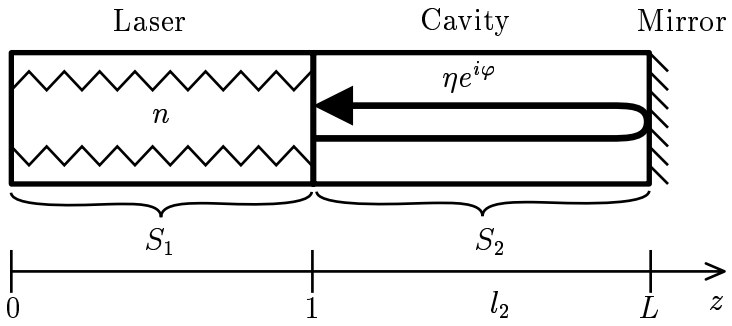

Figure 1: Geometric configuration for the case of a two-section laser. The DFB section S_1 (DFB=distributed feedback, i. e., $\kappa(z) \neq 0$ in (2)) acts as a laser. Its spatially averaged carrier density n is a scalar dependent variable. The other section acts as a cavity and provides delayed feedback of strength η and phase φ.

which reads as follows:

$$\frac{d}{dt}\psi(t,z) = \sigma\partial_z\psi(t,z) + \beta(n(t),z)\psi(t,z) - i\kappa(z)\sigma_c\psi(t,z) + \rho(z)p(t,z) \tag{2}$$

$$\frac{d}{dt}p(t,z) = (i\Omega_r(z) - \Gamma(z)) \cdot p(t,z) + \Gamma(z)\psi(t,z) \tag{3}$$

$$\frac{d}{dt}n(t) = I - \frac{n(t)}{\tau} - P \cdot \Big[(G(n(t)) - \rho_1)(\psi(t),\psi(t))_1 + \rho_1 \operatorname{Re}(\psi(t),p(t))_1\Big] \tag{4}$$

where $\sigma = \left(\begin{smallmatrix} -1 & 0 \\ 0 & 1 \end{smallmatrix}\right)$ and $\sigma_c = \left(\begin{smallmatrix} 0 & 1 \\ 1 & 0 \end{smallmatrix}\right)$ and ψ satisfies reflection boundary conditions:

$$\psi_1(t,0) = r_0\psi_2(t,0), \quad \psi_2(t,L) = r_L\psi_1(t,L) \tag{5}$$

where $|r_0|, |r_L| < 1$ and $r_0 r_L \neq 0$. For brevity, we introduced the notation

$$(\psi,\varphi)_1 = \int_0^1 \psi(z)^*\varphi(z)\,dz$$

for ψ, $\varphi \in \mathbb{L}^2([0,L];\mathbb{C}^2)$ in (4).
The coefficients $\beta \in \mathbb{C}$, $\kappa \in \mathbb{R}$, $\rho \in \mathbb{R}$, $\Omega_r \in \mathbb{R}$ and $\Gamma \in \mathbb{R}$ ($\rho \geq 0$, $\Gamma > 0$) are section-wise spatially constant functions. We refer to their value in section S_k by the according index (e. g., ρ_1). Moreover, β_1 depends on n in the following way:

$$\beta_1(n) = \beta_1^0 + (1 + i\alpha)G(n) - \rho_1 \tag{6}$$

where $\beta_1^0 \in \mathbb{C}$ ($\operatorname{Re}\beta_1^0 < 0$) and $\alpha > 0$. For simplicity[1], we assume that $G(n)$ is affine:

$$G(n) = g_1 \cdot (n-1) \qquad \text{where } g_1 > 0. \tag{7}$$

[1]Most of the assumptions are made to simplify the presentation. The computations presented in this paper can be done in a more general framework, i. e., more sections, other coefficients depending on n, etc.

It is obvious that system (2)–(4) has the form (1) where $E = (\psi, p)$. The linear differential operator $H(n)$ is defined by

$$H(n)\begin{pmatrix}\psi\\ p\end{pmatrix} = \begin{pmatrix}\sigma\partial_z + \beta(n) - i\kappa\sigma_c & \rho\\ \Gamma & (i\Omega_r - \Gamma)\end{pmatrix}\begin{pmatrix}\psi\\ p\end{pmatrix} \tag{8}$$

and acts from

$$Y := \{(\psi, p) \in \mathbb{H}^1([0,L];\mathbb{C}^2) \times \mathbb{L}^2([0,L];\mathbb{C}^2) : \psi \text{ satisfying (5)}\} \tag{9}$$

into $X = \mathbb{L}^2([0,L];\mathbb{C}^4)$. The coefficients κ, Γ, $\beta(n)$, Ω_r and ρ are bounded linear operators in $\mathbb{L}^2([0,L];\mathbb{C}^2)$ defined by the corresponding coefficients in (2)–(4). The hermitian form $g(n)[E,E]$ is defined by

$$g(n)\left[\begin{pmatrix}\psi\\ p\end{pmatrix}, \begin{pmatrix}\varphi\\ q\end{pmatrix}\right] = \int_0^1 (\psi^*(z), p^*(z)) \begin{pmatrix} G(n)-\rho_1 & \frac{1}{2}\rho_1 \\ \frac{1}{2}\rho_1 & 0\end{pmatrix}\begin{pmatrix}\varphi(z)\\ q(z)\end{pmatrix} dz.$$

Finally, we define the small parameter ε and the function $f(n)$ in (1) by $\varepsilon f(n) = I - n/\tau$ observing that I and τ^{-1} are of order $O(10^{-2})$ (see Tab. 1 and appendix A). Time t and space z are scaled in system (1) such that the speed of light within the device is 1 and the length of section S_1 is 1. Moreover, n is measured in multiples of the *transparency density* (the zero of $G(n)$) and E is scaled such that the factor P in (2) is actually ε. In this scaling, we have typically $\Gamma_1 \gg 1$ whereas the real parts of β are of order $O(1)$.
Furthermore, we have $\kappa_2 = \rho_2 = 0$ in the particular situation considered in this paper (non-dispersive feedback, see Fig. 1 and introduction). Hence, the amount η and the phase φ of the feedback from section S_2 can be varied by changing modulus and phase of r_L and we can set $\beta_2 = \Omega_{r,2} = \Gamma_2 = 0$ without loss of generality.

2.2 Model reduction

The following statements have been proved in [20] for the evolution system (1):

Theorem 1 (Existence of semiflow) *Let $|r_0|, |r_L| \le 1$, $\operatorname{Re}\beta_1^0 < 0$, $(E^0, n^0) \in V := \mathbb{L}^2([0,L];\mathbb{C}^4) \times \mathbb{R}$. Then, system (1) generates a strongly continuous semiflow $S(t,(E^0,n^0))$ in V which depends C^∞ smoothly on its initial values and on all parameters for all $t \ge 0$. If $E^0 \in Y$, then $S(t,(E^0,n^0))$ is a classical solution of (1), i. e., $(E(t),n(t)) = S(t,E^0,n^0)$ is continuously differentiable with respect to t and $E(t) \in Y$ for all $t \ge 0$.*

This theorem guarantees that (1) is indeed an infinite-dimensional dynamical system, i .e., its solutions exist for all positive times.
The next statement investigates the spectrum of $H(n)$ for fixed n and the strongly continuous semigroup $T(t)$ (which is actually a group) in X generated by H.

Theorem 2 (Spectral properties of $H(n)$)
Let $\xi > \xi_- := \max\left\{-\Gamma_1, \frac{1}{L}\operatorname{Re}\left(\beta_1 - \frac{1}{2}\log(r_0 r_L)\right)\right\}$. Then, X can be decomposed into

two $T(t)$-invariant subspaces $X = X_+ \oplus X_-$ where X_+ is at most finite-dimensional and spanned by the eigenvectors associated to the eigenvalues of H in the right half-plane $\{\lambda : \operatorname{Re}\lambda \geq \xi\}$. The restriction of $T(t)$ to X_- is bounded according to

$$\|T(t)|_{X_-}\| \leq Me^{\xi t} \qquad \text{for } t \geq 0$$

in any norm which is equivalent to the X-norm (the constant depends on the particular choice of the norm). The subspace X_+ is nontrivial if ξ is sufficiently close to ξ_-.

Moreover, we know that the eigenvalues of $H(n)$ can be computed as roots of its characteristic function $h(\cdot, n)$:

Lemma 3 (Computation of eigenvalues of $H(n)$) *A complex number $\lambda > \xi_-$ is an eigenvalue of $H(n)$ if and only if*

$$0 = h(\lambda, n) = \left(\eta e^{2\pi i\varphi - 2\lambda l_2}, -1\right) T_1(1; \lambda, n) \begin{pmatrix} r_0 \\ 1 \end{pmatrix}.$$

Here, we denoted

$$T_1(z; \lambda, n) = \frac{e^{-\gamma z}}{2\gamma} \begin{pmatrix} \gamma + \mu + e^{2\gamma z}(\gamma - \mu) & i\kappa_1 \left(1 - e^{2\gamma z}\right) \\ -i\kappa_1 \left(1 - e^{2\gamma z}\right) & \gamma - \mu + e^{2\gamma z}(\gamma + \mu) \end{pmatrix}$$

for $z \in [0, 1]$ where $\mu = \lambda - \rho_1\Gamma_1(\lambda - i\Omega_{r,1} + \Gamma_1)^{-1} - \beta_1(n)$ and $\gamma = \sqrt{\mu^2 + \kappa_1^2}$.

If $n < 1$ and $|r_L| < 1$, all eigenvalues λ of $H(n)$ are in the left half-plane $\{\operatorname{Re}\lambda < 0\}$. For increasing n, finitely many of them will cross the imaginary axis according to theorem 2. Denote the smallest n where $q \geq 1$ eigenvalues λ of $H(n)$ are on the imaginary axis by n_0 (*threshold* carrier density). Choose $\xi < 0$ such that all other (non purely imaginary) eigenvalues of $H(n_0)$ lie to the left of the line $\{\operatorname{Re}\lambda = \xi\}$. We denote the space X_+ of complex dimension q according to theorem 2 by $X_c(n)$ and define the spectral projection $P_c(n)$ for $H(n)$ onto $X_c(n)$. $P_c(n)$ depends smoothly on n in a neighborhood of n_0. Let $B(n)$ be a smooth basis of $X_c(n)$.
According to [20], the following local center manifold theorem holds in the vicinity of n_0 (This theorem is based on the general result in [27]):

Theorem 4 (Model reduction) *Let $k > 2$ be an integer number and $C > 0$. Let $\varepsilon_0 > 0$ be sufficiently small and U be a sufficiently small neighborhood of n_0 (depending on C and k). Define the balls*

$$\begin{aligned} \mathcal{B} = &\ \{(E_c, n) \in \mathbb{C}^q \times \mathbb{R} : \|E_c\| < C, n \in U)\} \subset \mathbb{C}^q \times \mathbb{R} \text{ and} \\ \mathcal{N} = &\ \{(E, n) \in X \times \mathbb{R} : \|E\| < C, n \in U\} \subset X \times \mathbb{R}. \end{aligned}$$

Then, there exists a manifold $\mathcal{C}$ with the following properties:

1. (Representation) *$\mathcal{C}$ can be represented as the graph of a map from $\mathcal{B}$ into $\mathcal{N}$ which maps $(E_c, n) \in \mathcal{B}$ to $(B(n)E_c + \varepsilon\nu(E_c, n, \varepsilon), n)$ where $\nu : \mathcal{B} \times (0, \varepsilon_0) \to X$ is C^k with respect to all arguments. Denote the E-component of $\mathcal{C}$ by $E_X(E_c, n, \varepsilon) = B(n)E_c + \varepsilon\nu(E_c, n, \varepsilon) \in X$.*

2. (Invariance) *$\mathcal{C}$ is $S(t,\cdot)$-invariant relative to $\mathcal{N}$ if $\varepsilon < \varepsilon_0$.*

3. (Exponential attraction) *Let (E,n) be such that $S(t,(E,n)) \in \mathcal{N}$ for all $t \geq 0$. Then, there exists a $(E_c,n_c) \in \mathcal{B}$ such that for some $M > 0$*

$$\|S(t,(E,n) - S(t,(E_X(E_c,n_c,\varepsilon),n_c))\| \leq Me^{\xi t} \qquad \text{for all } t \geq 0. \tag{10}$$

4. (Flow) *The values $\nu(E_c,n,\varepsilon)$ are in Y and their $P_c(n)$-component is 0 for all $(E_c,n,\varepsilon) \in \mathcal{B}$. The flow on $\mathcal{C}$ is differentiable with respect to t and governed by the ODEs*

$$\begin{aligned} \frac{d}{dt}E_c &= H_c(n)E_c + \varepsilon a_1(E_c,n,\varepsilon)E_c + \varepsilon^2 a_2(E_c,n,\varepsilon)\nu \\ \frac{d}{dt}n &= \varepsilon F(E_c,n,\varepsilon) \end{aligned} \tag{11}$$

where

$$\begin{aligned} H_c(n) &= B(n)^{-1}H(n)P_c(n)B(n) \\ a_1(E_c,n,\varepsilon) &= -B(n)^{-1}P_c(n)\partial_n B(n)F(E_c,n,\varepsilon) \\ a_2(E_c,n,\varepsilon) &= B^{-1}(n)\partial_n P_c(n)F(E_c,n,\varepsilon)(Id - P_c(n)) \\ F(E_c,n,\varepsilon) &= f(n) - g(n)\left[E_X(E_c,n,\varepsilon),E_X(E_c,n,\varepsilon)\right]. \end{aligned}$$

System (11) is symmetric with respect to rotation $E_c \to E_c e^{i\varphi}$ and ν satisfies $\nu(e^{i\varphi}E_c,n,\varepsilon) = e^{i\varphi}\nu(E_c,n,\varepsilon)$ for all $\varphi \in [0,2\pi)$.

We observe that the only unknown term $\nu(E_c,n,\varepsilon)$ enters E_X with a factor ε in front. Hence, ν enters system (11) with a factor of order $O(\varepsilon^2)$. Consequently, the replacement of ν by 0 is a regular perturbation of (11) preserving the rotational symmetry of (11). The approximate system is called *mode approximation* and reads

$$\begin{aligned} \frac{d}{dt}E_c &= H_c(n)E_c + \varepsilon a(E_c,n)E_c \\ \frac{d}{dt}n &= \varepsilon F_0(E_c,n) \end{aligned} \tag{12}$$

where

$$\begin{aligned} H_c(n) &= B(n)^{-1}H(n)P_c(n)B(n) \\ a(E_c,n) &= -B(n)^{-1}P_c(n)\partial_n B(n)F_0(E_c,n) \\ F_0(E_c,n,) &= f(n) - g(n)\left[B(n)E_c,B(n)E_c\right]. \end{aligned}$$

The matrix $H_c(n)$ is a representation of $H(n)$ restricted to its critical subspace $X_c(n)$ in some basis $B(n)$. The matrix H_c depends on the particular choice of $B(n)$ but its spectrum coincides with the critical spectrum of $H(n)$. The term $\varepsilon a E_c$ appears since the space X_c depends on time t. Any normally hyperbolic invariant manifold (e. g., fixed point, periodic orbit, invariant torus) which is present in the dynamics of (12) persists under the perturbation $O(\varepsilon^2)\nu$. Hence, it is also present in system (11) describing the flow on the invariant manifold $\mathcal{C}$ and in the semiflow of the complete system (1). Furthermore, its hyperbolicity and the exponential attraction towards $\mathcal{C}$ ensure its continuous dependence on small parameter perturbations.

2.3 Particular choice of parameters

The mode approximations (12) derived in section 2.2 allow for detailed studies of their long-time behavior since they are low-dimensional ordinary differential equations. Several analytic and computational results have been obtained previously about the existence regions of *self-pulsations* ([3], [6], [25], [31]) and its synchronization properties [5] using the single-mode approximation (see section 3).
The particular form of system (12) depends on the the number q of critical eigenvalues on the imaginary axis at the threshold n_0. We restrict our interest to cases where the number q of critical eigenvalues of H is at most 2.
Furthermore, we adjust the relative resonance frequency of the material $\Omega_{r,1}$ in the following manner: The solitary section S_1 with zero facet reflectivities, gain dispersion and feedback (i. e., $\rho_1 = r_0 = r_L = 0$) is symmetric with respect to reflection. Thus, if $H(n)$ has the eigenvalue $\lambda + i \operatorname{Im}\beta_1(n)$, it has also the eigenvalue $\bar{\lambda} + i \operatorname{Im}\beta_1(n)$. Typically, a pair of eigenvalues becomes critical having the frequencies $\operatorname{Im}\lambda_{1,2} \approx \operatorname{Im}\beta_1(n_0) \pm \kappa_1$. The frequency region $(\operatorname{Im}\beta_1 - \kappa_1, \operatorname{Im}\beta_1 + \kappa_1)$ is usually referred to as the *stopband* of the active section. Hence, the solitary section S_1 can have stable *on-states* (i. e., rotating-wave solutions, relative equilibria of (1)) at both ends of the stopband. We break the reflection symmetry by choosing $\rho_1 > 0$ and $\Omega_{r,1}$ outside of the stopband frequency region. Then, the slope of the gain curve (see appendix A) favours frequencies closer to $\Omega_{r,1}$ such that the solitary active section S_1 has a distinct stable on-state at the threshold n_0.

$l_1 = 1$	$l_2 = 1.136$	$r_0 = 10^{-5}$	$r_L = \eta e^{2\pi i\varphi}$
$d_1 = -0.275$	$d_2 = 0$	$\kappa_1 = 3.96$	$\kappa_2 = 0$
$g_1 = 2.145$	$g_2 = \rho_2 = 0$	$\alpha_1 = 5$	$\rho_1 = 0.44$
$\Gamma_1 = 90$	$\Omega_1 = -20$	$I = 6.757 \cdot 10^{-3}$	$\tau = 3.59 \cdot 10^2$

Table 1: Choice of parameters for the bifurcation diagrams presented in sections 3 and 4.

We choose the feedback phase and strength as our primary bifurcation parameters and deploy numerical continuation methods [8] to explore the bifurcation diagram in the two-parameter plane keeping all other parameters fixed according to Tab. 1. We can do so by varying the absolute value η and the phase φ of $r_L := \eta e^{2\pi i\varphi}$ setting $\beta_2 = 0$ without loss of generality.
In order to obtain the coefficients of (12), we have to compute the following quantities:

- The critical eigenvalues λ_j are roots of the characteristic function h of $H(n)$ defined in lemma 3. We include n, η and φ as parameters to emphasize that λ_j depends on them (see section 2.2):

$$0 = h(\lambda_j, n, \eta, \varphi) = \left(\eta e^{2\pi i\varphi - 2\lambda_j l_2}, -1\right) T_1(1; \lambda_j, n) \begin{pmatrix} r_0 \\ 1 \end{pmatrix}.$$

- The eigenvector $v_j = (\psi_j, p_j)$ corresponding to λ_j and its adjoint $v_j^\dagger = (\psi_j^\dagger, p_j^\dagger)$ are defined (up to a scaling) by (see [5], [31] for the adjoint)

$$\begin{pmatrix}\psi_j\\ p_j\end{pmatrix} = \begin{pmatrix} T(z,0;\lambda_j,n)\begin{pmatrix}r_0\\1\end{pmatrix} \\ \frac{\Gamma}{\lambda_j - i\Omega_r + \Gamma} T(z,0;\lambda_j,n)\begin{pmatrix}r_0\\1\end{pmatrix}\end{pmatrix} \qquad \begin{pmatrix}\psi_j^\dagger\\ p_j^\dagger\end{pmatrix} = \begin{pmatrix} \begin{pmatrix}\bar\psi_{j,2}\\ \bar\psi_{j,1}\end{pmatrix} \\ \frac{\rho}{\Gamma}\begin{pmatrix}\bar p_{j,2}\\ \bar p_{j,1}\end{pmatrix}\end{pmatrix} \tag{13}$$

  if λ_j is algebraically simple. In (13), $T(z,0;\lambda_j,n) = T_1(z;\lambda_j,n)$ if $z \le 1$ and

$$T(z,0;\lambda_j,n) = \begin{pmatrix} e^{-\lambda_j z} & 0 \\ 0 & e^{\lambda_j z}\end{pmatrix} T_1(1;\lambda_j,n) \quad \text{if } z \ge 1.$$

3 The single-mode case

3.1 Definition of the system

Firstly, we consider the generic case where a single eigenvalue λ of $H(n)$ is on the imaginary axis ($q = 1$). Since we have chosen the configuration of the active section S_1 such that it has only one stable on-state at $\eta = 0$, this model is certainly valid for sufficiently small η in the vicinity of n_0. Since λ is uniformly isolated, it depends smoothly on n and all parameters. The term a in (12) vanishes if we scale the eigenvector (ψ, p) such that

$$\left(\begin{pmatrix}\psi^\dagger\\ p^\dagger\end{pmatrix}, \begin{pmatrix}\psi\\ p\end{pmatrix}\right) = 1$$

for all n under consideration. Moreover, we can decouple the phase of the complex quantity E_c in (12) due to the rotational symmetry of the system. Hence, we have to analyse a system for $S = |E_c|^2$, n and λ which reads as follows:

$$\dot S = 2\,\mathrm{Re}(\lambda) S \tag{14}$$

$$\dot n = \varepsilon\,(I_1 - n - R(\lambda, n, \varphi, \eta) S) \tag{15}$$

$$0 = \ h(\lambda, n, \varphi, \eta) \tag{16}$$

where $\varepsilon = \tau^{-1}$, $I_1 = I\tau$, and the coefficient R is defined as follows:

$$R(\lambda, n, \varphi, \eta) = [G(n) - \rho_1 + \mathrm{Re}\,\chi_1(\lambda)](\psi, \psi))_1^2$$

(see appendix A for the definition of χ).
On-states are equilibria of (14)–(16) whereas periodic solutions of (14)–(16) represent quasiperiodic solutions of (12). This type of modulated rotating wave solutions is typically referred to as *self-pulsations*. System (14)–(16) is an implicit differential equation (or differential-algebraic equation, DAE). Its inherent dynamical system is two-dimensional. Standard numerical continuation software like, e. g., AUTO [8]

is not able to treat DAEs directly. However, we can easily convert (14)–(16) to an equivalent explicit system of ODEs by changing (16) to

$$\dot{\lambda} = -\frac{\partial_2 h(\lambda, n, \varphi, \eta)\dot{n} + c \cdot h(\lambda, n, \varphi, \eta)}{\partial_1 h(\lambda, n, \varphi, \eta)} \tag{17}$$

if λ is an isolated simple root of h. For sufficiently large $c > 0$, (14), (15), (17) is a four-dimensional ODE which has a stable invariant manifold defined by $h = 0$. On this invariant manifold, the flow is identical to the flow of (14)–(16). The transformation of (16) into (17) is sometimes referred to as Baumgarte regularization [7].

3.2 The Bifurcation Diagram

We explore the dynamics numerically in the two-parameter plane (φ, η) choosing the other parameters according to the example presented in [29] (see Tab. 1) The procedure is as follows: Firstly, we choose a very small feedback level $\eta = 0.1$ and report the smallest n_0 such that $H(n_0)$ possesses an eigenvalue on the imaginary axis for $\varphi = 0$, i.e., $h(\cdot, n_0, 0, \eta)$ has a purely imaginary root. This is $n_0 = 1.316194$ for the parameter situation outlined in Tab. 1. The corresponding root of h is $\lambda = -1.632607i$. We consider only this eigenvalue λ of H and its eigenvector ψ in (16) from now. There exists an equilibrium with $S = (I_1 - n_0)/R(\lambda, n_0, 0, \eta)$ and $n = n_0$.

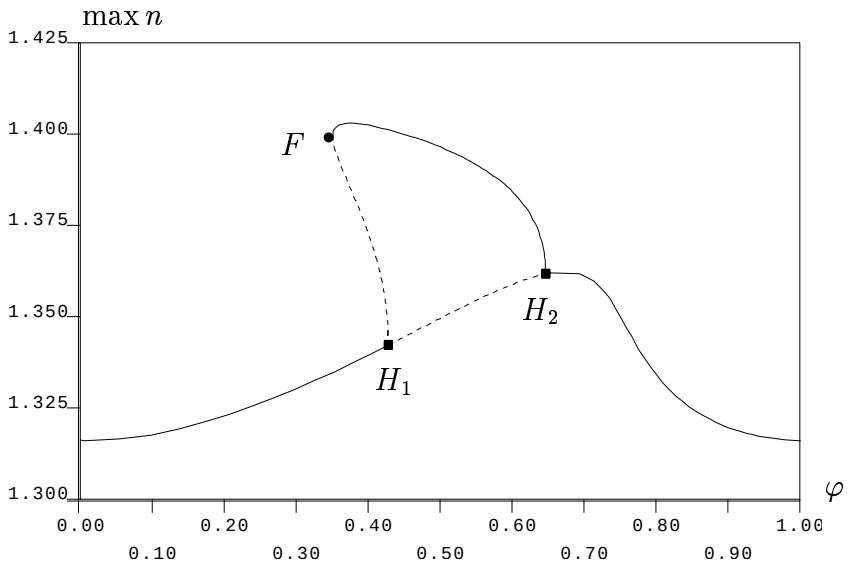

Figure 2: Bifurcation diagram for $\eta = 0.1$. We report the n-component for the on-state and the maximum of the n-component for the periodic solutions.

In the next step, we report how this equilibrium changes its location in phase space and its stability under variation of φ (see Fig.2). We observe that the threshold is

slightly modulated according to the phase of the feedback. Moreover, the equilibrium looses its stability at the point H_1 and regains stability at H_2 in a Hopf bifurcation. We obtain a family of stable periodic solutions ending in the supercritical Hopf point H_2 and a family of unstable periodic solutions ending in the subcritical Hopf point H_1. Both families of periodic solutions annihilate each other in a saddle-node bifurcation of limit cycles at F. Note that the location of the equilibrium coincides exactly with the location of corresponding rotating-wave solution of the complete system (1).

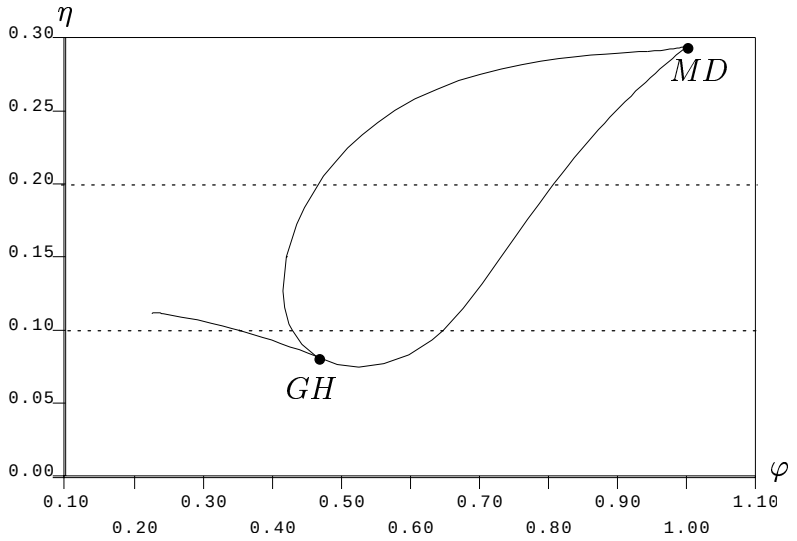

Figure 3: Location of Hopf and saddle-node of limit cycle parameter values in the (φ, η)-plane. The one-dimensional bifurcation diagrams of Fig. 2 and Fig. 4 have been obtained along the horizontal dotted lines.

In the next run, we add η as a free parameter to compute the curve of Hopf points and the curve of the points where the saddle-node of limit cycles happens in the two-parameter plane (φ, η). The result is shown in Fig. 3. The saddle-node curve of limit cycles and the Hopf curve meet in a generalized Hopf point GH. Both ends of the Hopf curve meet in the point MD. The root λ has multiplicity 2 in the equilibrium at this parameter value. We refer to it as an equilibrium with *mode degeneracy* as λ is an eigenvalue of $H(n)$ of algebraic multiplicity 2. We explore the vicinity of this equilibrium using the two-mode approximation in section 4 since the number q of critical eigenvalues of $H(n)$ is 2 near MD. Indeed, the single-mode model (14)–(16) is discontinuous if $\partial_1 h = 0$ and the continuation stops indicating a numerical failure.

Starting from one of the Hopf points at $\eta = 0.2$, we draw another one-dimensional bifurcation diagram keeping $\eta = 0.2$ fixed but varying φ. The numerical result is shown in Fig. 4.

The line of equilibria has folded twice at F_1 and F_2 indicating saddle-node bifurcations. The family of periodic orbits starting from H_2 is stable and ends in a

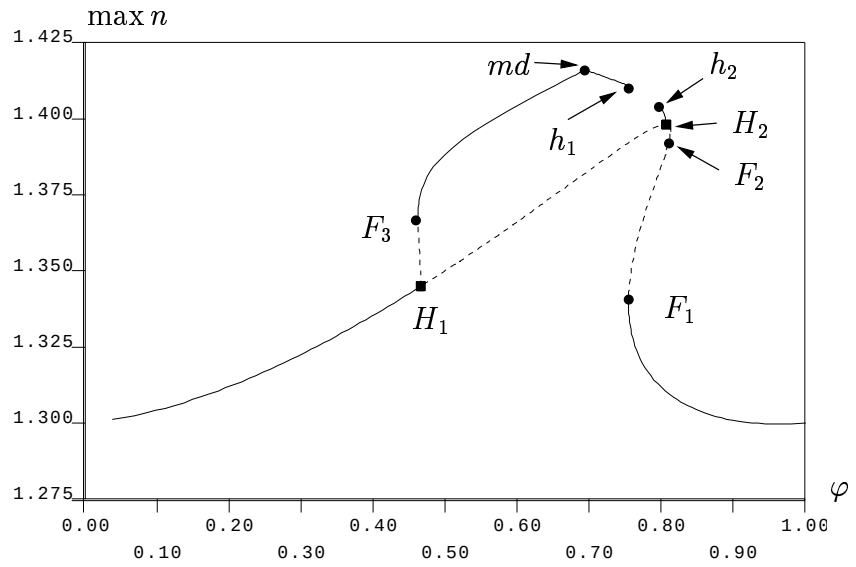

Figure 4: Bifurcation diagram at $\eta = 0.2$. We report the n-component for the on-state and the maximum of the n-component for the periodic solutions.

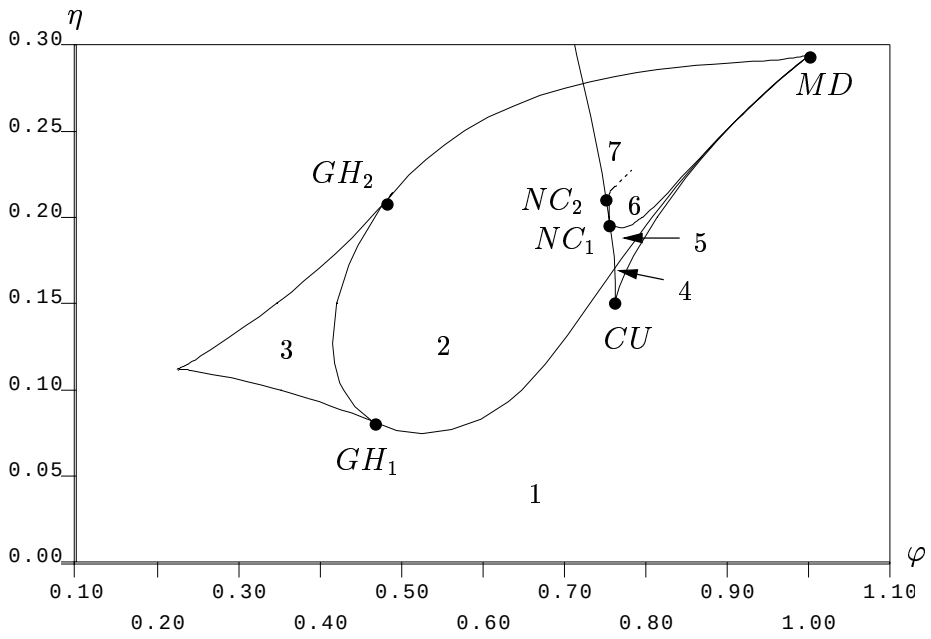

Figure 5: Bifurcation diagram in the two parameter plane (φ, η). Codimension 2 bifurcations are marked by black points and labels. GH refers to a generalized Hopf bifurcation, CU to a cusp bifurcation and NC to a non-central saddle-node on a closed orbit.

homoclinic bifurcation at h_2. The family of periodic orbits starting from H_1 is unstable and collides with a stable branch in the saddle-node bifurcation of limit cycles F_3. Continuating the stable branch of periodic solutions starting from F_3, we hit a

discontinuity of the model at md. There, the periodic orbit comes close to a point in the phase plane where λ is not an isolated root of $h(\cdot, n)$ anymore. Hence, there is no *continuous* family of periodic orbits between h_1 and F_3.

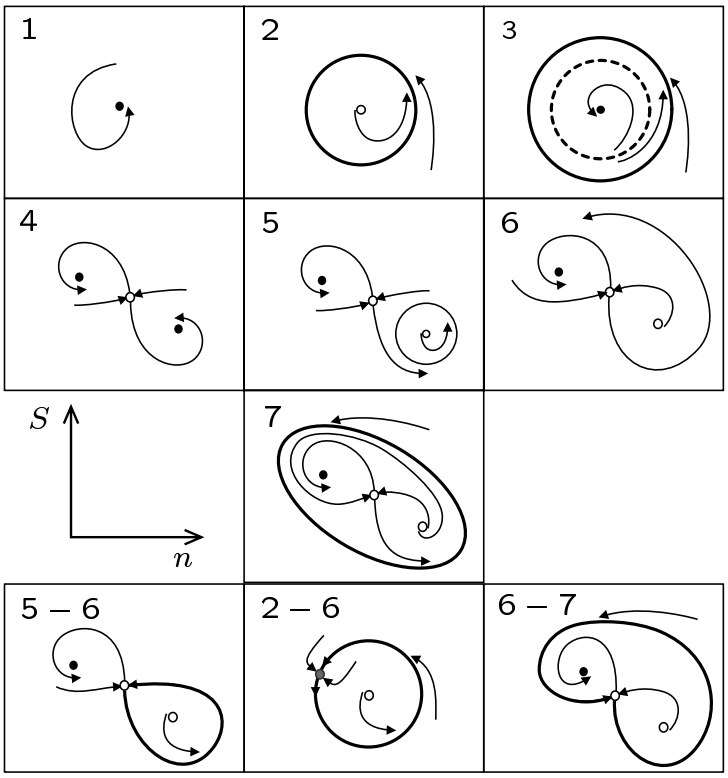

Figure 6: Symbolic phase-portrait sketches for the regions 1 *to* 7 *of Fig. 5. In addition, we display the homoclinic bifurcations between the regions* 2, 5, 6 *and* 7. *Black points symbolize stable equilibria, white points are unstable equilibria. If an unstable equilibrium is a saddle, we sketch the stable and unstable manifolds. The gray equilibrium in case* 2–6 *is a saddle-node. Stable periodic orbits and homoclinics are thick solid lines, unstable periodic orbits are dashed solid lines. The additional arrows show the behavior of the vector field.*

In the last step, we continuate the saddle-node points F_1 and F_3 and the homoclinic[2] h_2 varying both parameters, η and φ. Fig. 5 shows the two-parameter bifurcation diagram and Fig. 6 the corresponding symbolic phase portrait sketches. We note that the two saddle-node bifurcations observed in Fig. 4 emanate from a cusp bifurcation at CU in Fig. 5. Moreover, the curve of homoclinics in the (φ, η)-plane starting from h_2 at $\eta = 0.2$ (Fig. 4) turns back to $\eta = 0.2$ (at h_1, see Fig. 4). Along this curve, the homoclinic undergoes an orbit flip scenario: a parameter path of central saddle-nodes on closed orbits between two non-central saddle-nodes on closed orbits (NC_1–NC_2). It turns out that the saddle-node F_1 is actually situated on the homoclinic h_1 in Fig. 4. The region 6 in the vicinity of the central saddle-node on the closed orbit is a classical excitability scenario [13].

[2]Actually, we continuated periodic orbits of a fixed large period.

The continuation of the homoclinic curve in the plane (φ, η) ends at some distance after (above) the point NC_2 when the homoclinic approaches a point in the phase plane where λ is degenerate.
The curve of homoclinics, the Hopf curve and the saddle-node curve in Fig. 5 approach each other and become tangent at MD. However, this does not indicate the presence of a Takens-Bogdanov bifurcation since the model is discontinuous in the vicinity of MD. Indeed, the Hopf frequency along the Hopf curve increases towards MD.

4 The two mode case

In this section, we explore in detail the neighborhood of MD from Fig. 5 completing the bifurcation diagram for larger feedback levels η. Let n_0 be a threshold carrier density where $H(n_0)$ has a dominating eigenvalue λ of algebraic multiplicity 2 on the imaginary axis. A n_0 of this type exists, e. .g, in the point $MD = (\varphi_0, \eta_0)$ of the parameter plane (φ, η) in section 3. Hence, the complex dimension q of the critical subspace X_c is 2 and the (real) dimension of the invariant manifold $\mathcal{C}$ is 5 (see section 2.2). In order to obtain the coefficients of system (12), we have to construct a basis $B(n)$ and a projector $P_c(n)$ which depend smoothly on n and the bifurcation parameters η and φ in the vicinity of n_0, φ_0 and η_0.

4.1 Definition of $B(n)$ and $P_c(n)$ — elimination of the absolute phase

Let λ_1 and λ_2 be the two roots of $h(\cdot, n, \varphi, \eta)$ which coincide and are situated on the imaginary axis if $n = n_0$, $\varphi = \varphi_0$ and $\eta = \eta_0$. For brevity, we denote the corresponding eigenvectors (ψ_j, p_j) by v_j and the adjoint eigenvectors by $v_j^\dagger$ $(j = 1, 2)$. The vectors v_j and $v_j^\dagger$ are defined by (13). Hence v_j and $v_j^\dagger$ depend analytically on λ_j.
We introduce the quantities

$$\begin{aligned} \theta &:= \frac{1}{2}(\lambda_1 + \lambda_2) \\ \mu &:= \frac{1}{4}(\lambda_1 - \lambda_2)^2, \end{aligned}$$

and define the basis $B = [u_1, u_2]$ by

$$\begin{aligned} u_1 &= \frac{v_1 - v_2}{\lambda_1 - \lambda_2} \\ u_2 &= \frac{1}{2}(v_1 + v_2). \end{aligned} \tag{18}$$

θ and μ depend smoothly on n, φ and η in the vicinity of the degeneracy MD. The vectors u_1 and u_2 do not change if we permute the eigenvalues λ_1 and λ_2. Moreover,

they are also smooth with respect to n, φ and η and uniformly linearly independent around the degeneracy point. We denote the ψ component of u_j by ξ_j $(j = 1, 2)$. The representation of H in the basis (u_1, u_2) reads:

$$Hu_1 = \theta u_1 + u_2 \qquad\qquad Hu_2 = \mu u_1 + \theta u_2. \tag{19}$$

Hence, the representation of H with respect to the basis (u_1, u_2) is smooth in the degeneracy point.
Furthermore, we define the functionals (for $x \in \mathbb{L}^2([0, L]; \mathbb{C}^4)$ and $y \in \mathbb{L}^2([0, L]; \mathbb{C}^2)$)

$$\begin{aligned}
P_1 x &= \frac{1}{2}\left(\frac{\lambda_1 - \lambda_2}{(v_1^\dagger, v_1)}(v_1^\dagger, x) + \frac{\lambda_2 - \lambda_1}{(v_2^\dagger, v_2)}(v_2^\dagger, x)\right) \\
P_2 x &= \frac{(v_1^\dagger, x)}{(v_1^\dagger, v_1)} + \frac{(v_2^\dagger, x)}{(v_2^\dagger, v_2)} \\
\Theta_j y &= (G(n) - \rho_1 + \chi_1(\lambda_j))(\psi_j, y)_1 \qquad (j = 1, 2), \\
Q_1 y &= \frac{\Theta_1 y - \Theta_2 y}{\bar{\lambda}_1 - \bar{\lambda}_2}, \qquad Q_2 y = \frac{1}{2}\left(\Theta_1 y + \Theta_2 y\right).
\end{aligned}$$

P_1 and P_2 as well as Q_1 and Q_2 are not affected by a permutation of λ_1 and λ_2. Since $P_j u_k = \delta_{jk}$, the functionals P_j are smoothly dependent on n and uniformly linearly independent around the degeneracy. We define

$$P_c x = P_1 x u_1 + P_2 x u_2.$$

Using these definitions of B and P_c, system (12) reads ($E_c = (x_1, x_2) \in \mathbb{C}^2$ and, hence, $x_j = P_j E_c$):

$$\begin{aligned}
\dot{x}_1 &= \theta(n)x_1 + \mu(n)x_2 - \dot{n}(P_1(n)\partial_n u_1(n)x_1 + P_1(n)\partial_n u_2(n)x_2) \\
\dot{x}_2 &= x_1 + \theta(n)x_2 - \dot{n}(P_2(n)\partial_n u_1(n)x_1 + P_2(n)\partial_n u_2(n)x_2) \\
\dot{n} &= \varepsilon\left[I_1 - n - \mathrm{Re}\left(|x_1|^2 Q_1\xi_1 + |x_2|^2 Q_2\xi_2 + \bar{x}_1 x_2 Q_1\xi_2 + \bar{x}_2 x_1 Q_2\xi_1\right)\right]
\end{aligned} \tag{20}$$

Finally, we observe that we can eliminate the absolute phase of the vector (x_1, x_2) due the rotational symmetry of system (20). We introduce the quantities

$$\begin{aligned}
r &= |x_1|^2 - |x_2|^2 \qquad (r \in \mathbb{R}), \\
\zeta &= \bar{x}_1 x_2 \qquad (\zeta \in \mathbb{C}).
\end{aligned}$$

Using r and ζ, we can easily recover the quantities

$$\begin{aligned}
|x_1|^2 &= \frac{1}{2}(\sqrt{r^2 + 4|\zeta|^2} + r), \\
|x_2|^2 &= \frac{1}{2}(\sqrt{r^2 + 4|\zeta|^2} - r).
\end{aligned}$$

Hence, system (20) has a 4-dimensional subsystem for r, ζ and n which reads as follows:

$$\begin{aligned}
\dot{r} &= 2\,\mathrm{Re}\left(b_{11}|x_1|^2 - b_{22}|x_2|^2 + (b_{12} - \bar{b}_{21})\zeta\right) \\
\dot{\zeta} &= b_{21}|x_1|^2 + \bar{b}_{12}|x_2|^2 + (\bar{b}_{11} + b_{22})\zeta \\
\dot{n} &= \varepsilon\left[I_1 - n - \mathrm{Re}\left(|x_1|^2 Q_1\xi_1 + |x_2|^2 Q_2\xi_2 + \zeta Q_1\xi_2 + \bar{\zeta} Q_2\xi_1\right)\right]
\end{aligned} \tag{21}$$

where the functions $b_{ij}(r,\zeta,n)$ are defined as

$$\begin{aligned} b_{11}(r,\zeta,n) &= \theta(n) - \dot{n}P_1(n)\partial_n u_1(n) & b_{12}(r,\zeta,n) &= \mu(n) - \dot{n}P_1(n)\partial_n u_2(n) \\ b_{21}(r,\zeta,n) &= 1 - \dot{n}P_2(n)\partial_n u_1(n) & b_{22}(r,\zeta,n) &= \theta(n) - \dot{n}P_2(n)\partial_n u_2(n). \end{aligned}$$

The functions $\theta(n)$ and $\mu(n)$ are given only implicitly by the root curves of $h(\cdot,n)$. We introduce θ and μ as new variables satisfying the differential equations

$$\begin{aligned} \dot{\theta} &= \frac{1}{2}\left(\dot{\lambda}_1 + \dot{\lambda}_2\right) \\ \dot{\mu} &= \frac{1}{2}\left(\dot{\lambda}_1 - \dot{\lambda}_2\right)(\lambda_1 - \lambda_2) \end{aligned} \tag{22}$$

in order to put the system in a form that is recognized by AUTO. In (22), the equations for $\dot{\lambda}_j$ are constructed in the same manner as (17). Assembling (21) and (22), we obtain a system of dimension 8 where the coefficients $P_i\partial_n u_j = P_i(\partial_n\theta\partial_\theta + \partial_n\mu\partial_\mu + \partial_n)u_j$ and $Q_i\xi_j$ depend on n, θ and μ. This system has a four-dimensional uniformly attracting invariant manifold where $\theta = \theta(n)$ and $\mu = \mu(n)$. We restrict our bifurcation analysis to this invariant manifold.

4.2 The bifurcation diagram

We explore the (φ,η)-plane in the same manner as in section 3. We start from a one-dimensional bifurcation diagram varying φ at $\eta = 0.1$ (see Fig. 7). This diagram

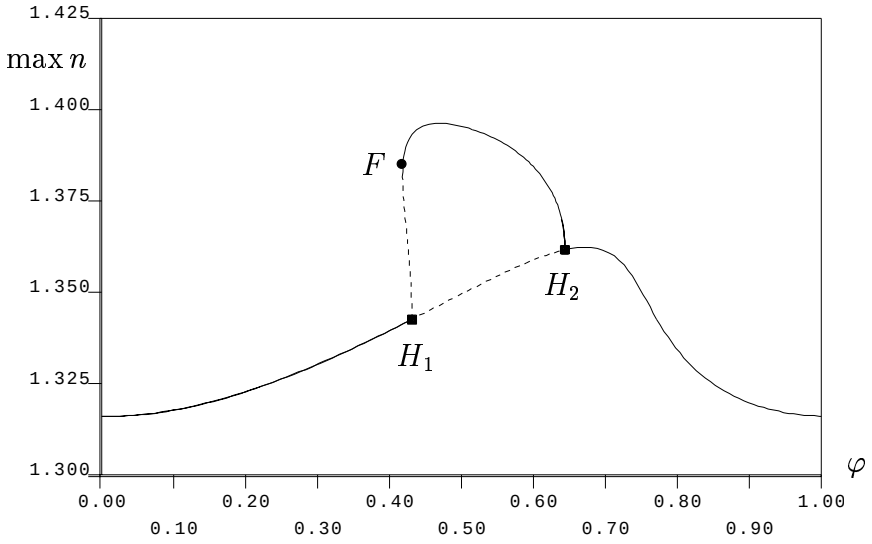

Figure 7: Bifurcation diagram for $\eta = 0.1$. We report the n-component for the on-state and the maximum of the n-component for the periodic solutions.

looks very similar to Fig. 2. Indeed, the locations of the equilibria coincide exactly and the stability of the equilibria as well as the location and the stability of the periodic solutions are in good quantitative correspondence.

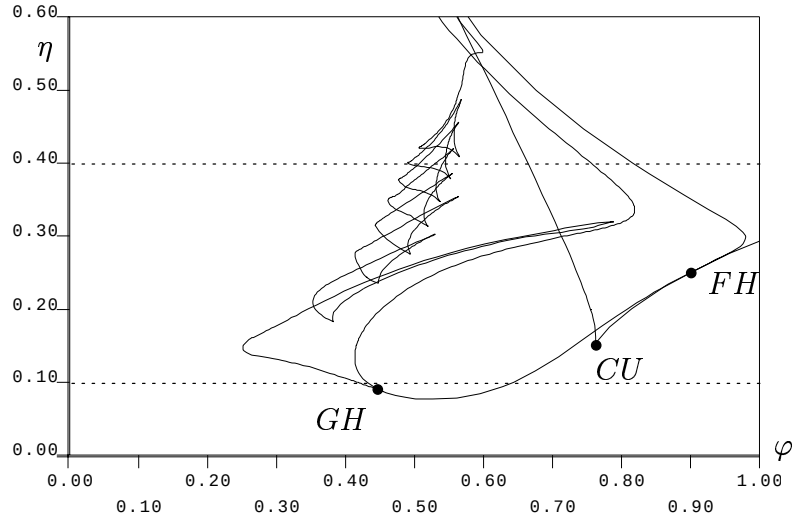

Figure 8: Location of Hopf and saddle-node of limit cycle bifurcations in the (φ, η)-plane. The one-dimensional bifurcation diagrams of Fig. 7 and Fig. 11 have been obtained along the horizontal dotted lines. This diagram should be compared to Fig. 3.

Again, we start from the bifurcation points in Fig. 7 to explore the (φ, η)-plane. Fig. 8 reports the location of the Hopf bifurcation and the curve of saddle-node bifurcations of limit cycles continuated from F. Furthermore, we know that the curve of saddle-node bifurcations of equilibria is identical with the corresponding curve in Fig. 5. Hence, we can insert this line into Fig. 8, too. The curve of saddle-nodes of limit cycles undergoes a sequence of cusps. To the left of this curve there exist periodic orbits in the parameter plane (coexisting with the stationary state).

We observe that the equilibrium with mode degeneracy MD is no longer a special point (except that it is situated on the saddle-node curve). However, one real eigenvalue changes its sign along the Hopf curve at the point FH in Fig. 8. FH is a fold-Hopf bifurcation of type "$s = 1, \theta < 0$" according to [15]. Fig. 9 shows the bifurcation diagram for the vicinity of FH enlarged. The line T of torus bifurcations emerging from FH according to theory is rather short ending in a $1:2$ resonance at a line PD of period doublings. Note that this bifurcation diagram is incomplete since there is a generically transversal heteroclinic structure emerging from FH (see [15] and references therein) which induces complicated dynamic behavior in the vicinity of FH.

Furthermore, we recompute the curve of homoclinic bifurcations shown in Fig. 5 and observe how the saddle-quantities change along the curve. The result is shown in Fig. 10. The configuration of the leading eigenvalues changes at the points labeled by SC_j in the following sequence: A stable pair of complex eigenvalues gets dominant at the point SC_1. The absolute value of its real part σ_s and the real part σ_u of the leading unstable eigenvalue satisfy the relation $\nu := -\sigma_u/\sigma_s < 1$. At the point SC_2 the saddle becomes neutral: $\nu = 1$. The real part of the divergence of the saddle $2\sigma_s + \sigma_u$ changes its sign to $+$ at the point SC_3, i. e., $\nu = 2$. Consequently, the

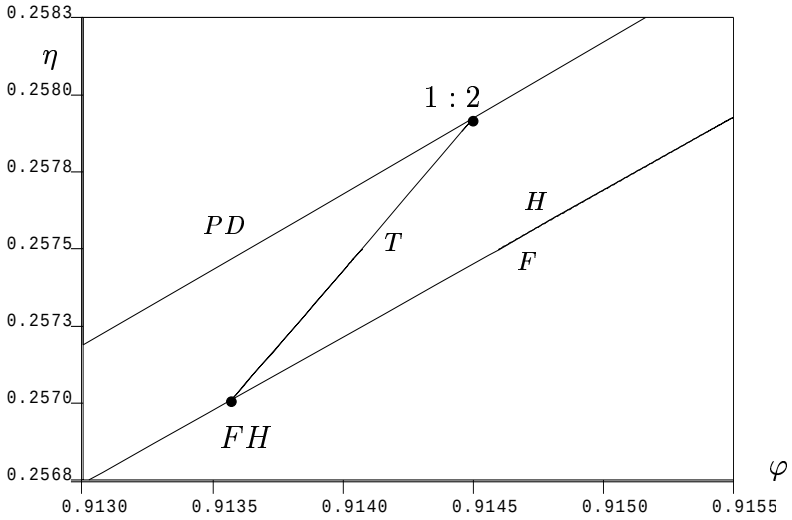

Figure 9: Local (incomplete) bifurcation diagram in the vicinity of the fold-Hopf interaction FH in the (φ, η)-plane.

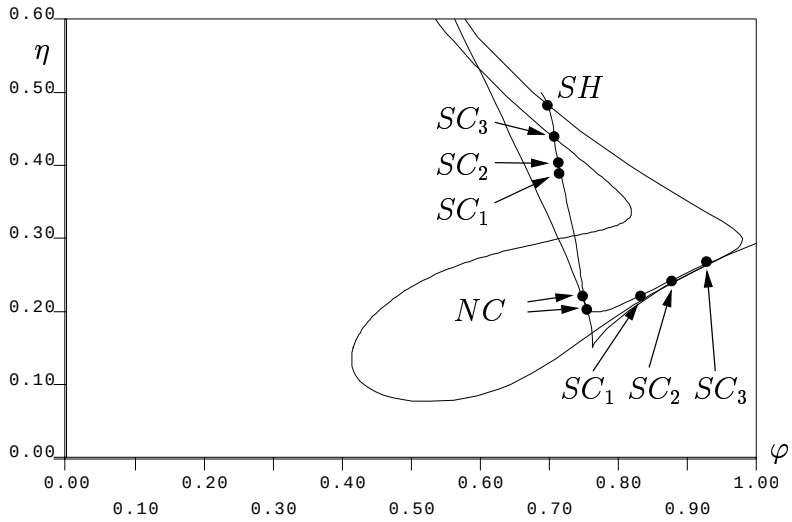

Figure 10: Location of the homoclinic bifurcation. The Hopf curve and the saddle-node curve are also drawn for orientation.

homoclinic connection changes its type at the point SC_1 into a saddle-focus homoclinic. The behavior in the vicinity of saddle-focus homoclinics includes complicated dynamics as described by Shilnikov's theorems [15]. Hence, the bifurcation diagram is incomplete at least "after" point SC_2 (there are n-loop homoclinics, period doublings, saddle-node bifurcations of periodic orbits, Smale-horseshoes etc., see [15]). The curve of homoclinics ends in a subcritical Shilnikov-Hopf bifurcation at SH.
In the next step, we draw the one-dimensional bifurcation diagram varying φ but keeping $\eta = 0.4$ fixed in Fig. 11. The Hopf point H_1 is supercritical and a family of periodic orbits connects to the other (saddle) Hopf point H_2. This family undergoes

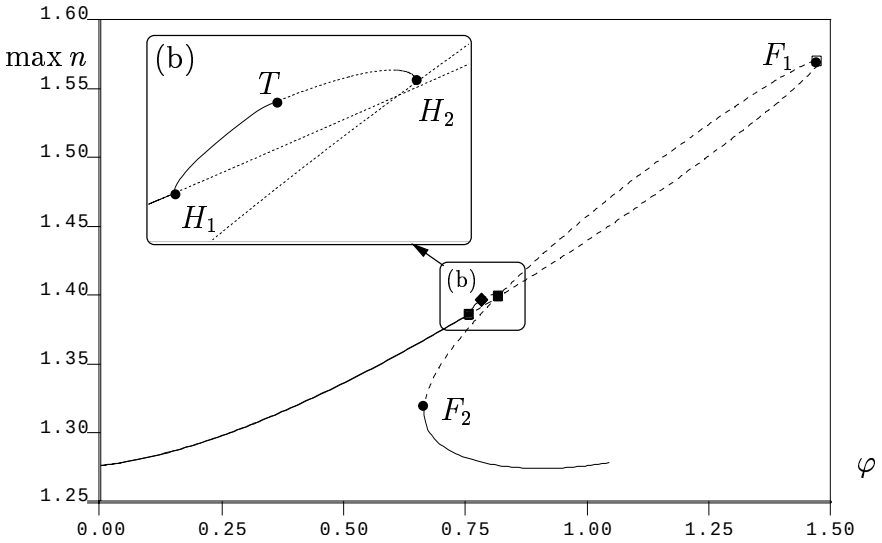

Figure 11: Bifurcation diagram for $\eta = 0.4$. Diagram (b) shows the framed region enlarged. We report the n-component for the on-state and the maximum of the n-component for the periodic solutions.

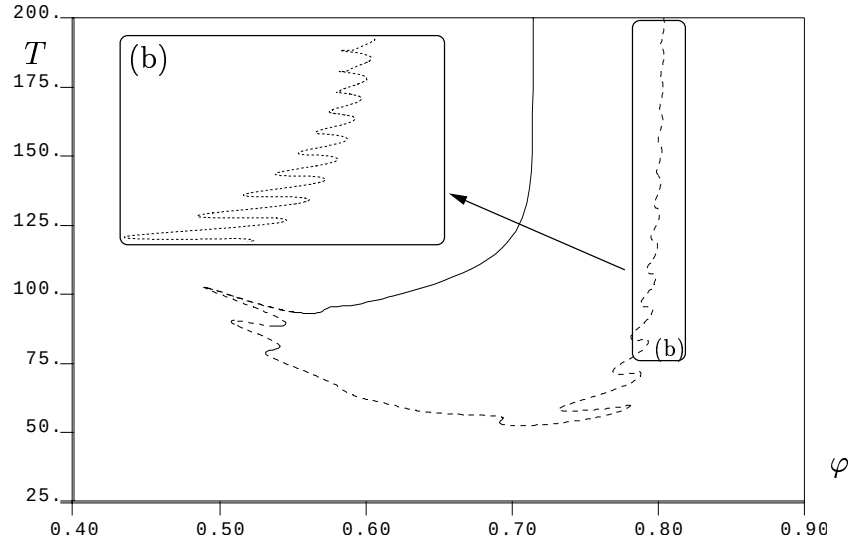

Figure 12: Family of periodic orbits at $\eta = 0.4$. Diagram (b) shows the framed region enlarged. This family has been omitted in Fig. 11. We report the period T for the periodic solutions. Stability/Instability is indicated by solid/dotted lines.

a torus bifurcation at T in between. Note that we have drawn the family of periodic solutions ending at the homoclinic (see Fig. 11) separately in Fig. 12 displaying the period T for varying φ. We observe that this family is not connected to the stationary states but it "ends" in a homoclinic connection to a "small" saddle periodic orbit from the family shown in Fig. 11.

The two disconnected families of periodic orbits visible for $\eta = 0.4$ in Fig. 11 and

Fig. 12 are referred to as different types of laser oscillations in the physics literature. The stable periodic orbits of Fig. 12 are undamped relaxation oscillations similar to the single-mode self-pulsations of section 3. Their frequency is slower than the asymptotic relaxation oscillation frequency due to their large amplitude and the proximity of a homoclinic. The other family of periodic orbits (shown in Fig. 11) has a small amplitude and a substantially higher frequency than the single-mode self-pulsations. They are often referred to as *self-pulsations of mode beating type* [22], [11]. Indeed, the Hopf frequency continually increases for increasing η along the left branch of the Hopf curve in Fig. 8.

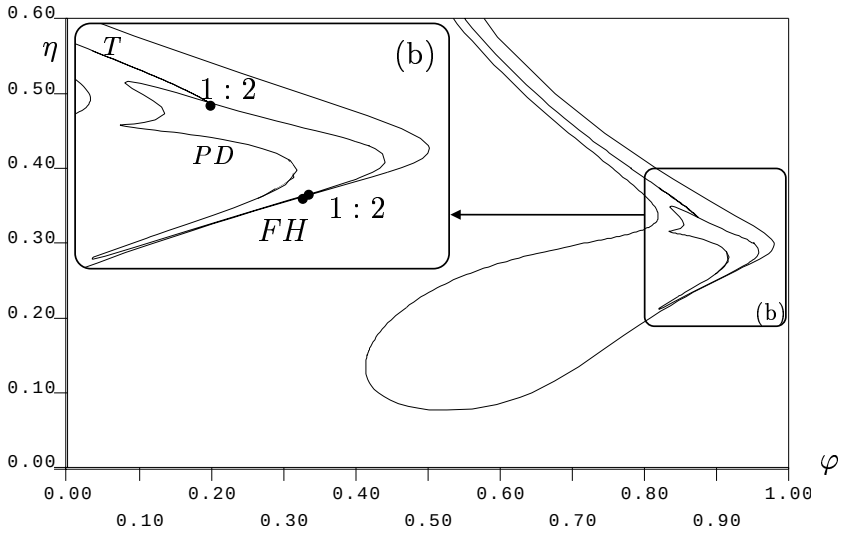

Figure 13: Torus (T) and period doubling (PD) bifurcations in the (φ, η)-plane. Diagram (b) shows the framed region enlarged. The region around FH is enlarged in Fig. 9. The Hopf curve is drawn for orientation.

Continuating the torus bifurcation T from Fig. 11, we obtain a line between the two Hopf lines of Fig. 8. This line T of torus bifurcations ends in a $1:2$ resonance at the point $1:2$ in Fig. 13. It approaches a period doubling curve PD which is also drawn in Fig. 13. The curve PD of period doublings appears also in Fig. 9 and passes through another $1:2$ resonance there.

If we continuate the family of saddle periodic orbits from the saddle Hopf point for some fixed $\eta > 0.257$ (the value of η for the point FH), we observe that the family ends in a homoclinic to a double-focus h (see Fig. 14 for $\eta = 0.3$). We show the continuation of this homoclinic in φ and η in Fig. 15. The saddle approached by the homoclinics is a double focus except in the small section between the two SC points where a single negative real eigenvalue is leading. Contraction is stronger than expansion at the saddle along the curve. This implies stable complicated dynamics in the vicinity of the double-focus homoclinics according to Shilnikov's theorems [15].

An remaining open question is: Where do the two families of periodic orbits (undamped relaxation oscillations and mode beating) meet each other? The two Hopf

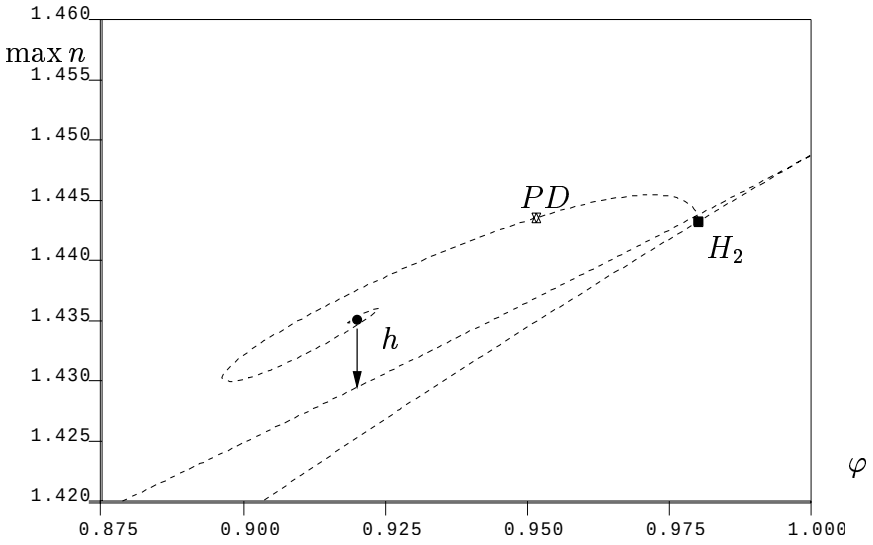

Figure 14: Bifurcation diagram for $\eta = 0.3$ (only part of the full phase period for φ. We report the n-component for the on-state and the maximum of the n-component for the periodic solutions. The arrow points to the saddle approached by the homoclinic h.

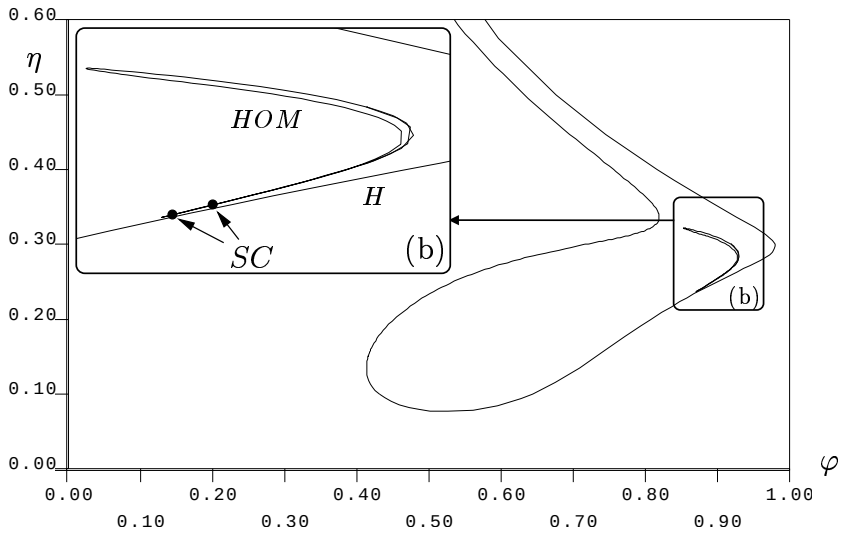

Figure 15: Curve of homoclinics in the (φ, η)-plane. Changes of saddle quantities along the curve are marked by SC. The Hopf curve is drawn for orientation.

points in Fig. 11 are both supercritical and connected by a family of periodic orbits. On the other hand, the Hopf points to the left of the generalized Hopf point GH (see Fig. 8) are subcritical and the family of periodic orbits emerging there ends in a homoclinic for $\eta > 0.2$. Hence, there must be another generalized Hopf point GH along the left Hopf curve. We detect it in Fig. 16 and draw the curve of saddle-nodes of periodic orbits emerging in GH. The framed region (c) of Fig. 16 shows how the family periodic orbits drawn in Fig. 12 disconnects from the family of equilibria.

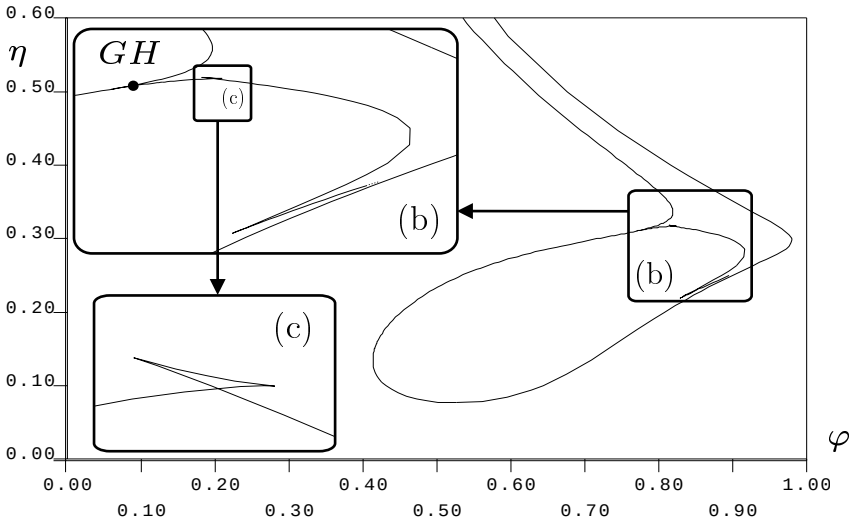

Figure 16: Curve of folds of periodic orbits in the (φ, η)-plane. The sub-plots (b) and (c) show the respective framed regions enlarged. The Hopf curve is drawn for orientation.

A family of periodic orbits approaching the double-focus homoclinic as shown in Fig. 14 undergoes a sequence of saddle-node bifurcations and period-doubling bifurcations. The saddle-node of limit cycles in Fig. 16 and the period doubling plotted as a curve in Fig. 13 are the first ones in this sequence.

5 Conclusions — Outlook

In this paper, we performed a numerical bifurcation analysis for a system of ODEs describing delayed-feedback phenomena in a semiconductor laser with short cavity. We constructed the model analytically in advance by reducing a singularly perturbed system of PDEs (the traveling-wave model with gain dispersion [20], [30]) to a local center manifold [20], [26]. The bifurcation parameters were the phase φ and the strength η of the delayed feedback.

In the first step, we analysed the single-mode dynamics for small η observing Hopf instabilities and two saddle-node curves of the equilibria (stationary lasing states). Moreover, the single-mode self-pulsations emerging at the Hopf bifurcation undergo a homoclinic bifurcation. A certain part of this homoclinic is actually a closed orbit to a saddle-node implying excitability [13] in the vicinity of the homoclinic.

In the second step, we extended our analysis to the neighborhood of the mode degeneracy point MD detected in the single-mode analysis using an appropriately posed two-mode system (a system of ODEs of dimension 4). We observed that there is a fold-Hopf interaction (a bifurcation of codimension 2) close to the point MD in the (φ, η)-plane and that the homoclinic connections change for larger η into saddle-focus homoclinics implying complicated dynamics according to Shilnikov's theorems. Furthermore, we found another type of self-pulsations often referred to

as mode beating. The two families of self-pulsations meet each other in a bifurcation close to a swallowtail of limit cycles (see Fig. 16).
In addition, we detected a torus bifurcation of the mode beating self-pulsations which ends in a strong $(1:2)$ resonance. The period doubling bifurcation crossing this strong resonance is only the first one in an infinite sequence accumulating to a curve of double-focus homoclinic connections. Again, Shilnikov's theorems imply stable complicated dynamics in the vicinity of these homoclinics.
Fig. 17 assembles all pictures concerning the (φ, η)-plane.

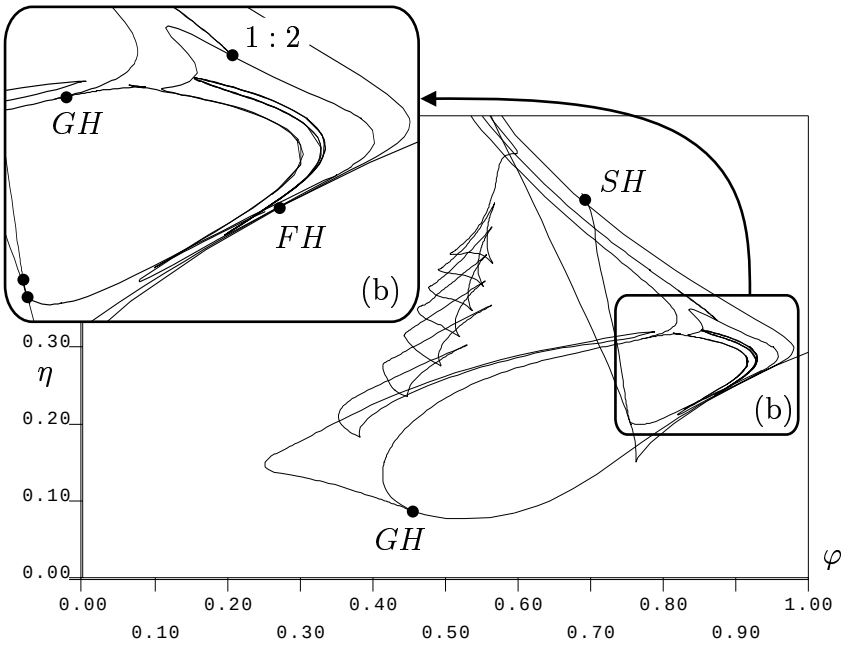

Figure 17: Bifurcation diagram in the (phi, η)-plane — Overview. Diagram (b) shows the framed region enlarged. The bifurcation of codimension 2 marked by black points and labels are explained in detail in the sections 3.2 and 4.2.

In summary, the map in the (φ, η)-plane (see Fig. 17) shows the roots and borders of many delayed-feedback phenomena observed experimentally and numerically [19], [29]. The diagram must remain incomplete since there is complicated dynamics inducing infinitely many bifurcations in the vicinity of some points (e. g., fold-Hopf interaction, strong resonance) and curves (e. g., homoclinic connections to saddle-focus or double-focus).
Of course, our future investigations will extend to other interesting experimental configurations, and a confirmation of the results presented in this paper by refined numerical continuation methods (HOMCONT [8]) and comparison to simulation results for the complete PDE system (1). Moreover, it is interesting to note that first examinations of the Lang-Kobayashi system using the methods outlined in this paper lead to similar bifurcation diagrams. This points to the mode degeneracy

of $H(n)$ which is common to both models as organizing center. Hence, it is worth studying the normal form for laser equations close to a mode degeneracy proposed by [26] in detail.

A Physical Interpretation of the Travelling-Wave Equations — Discussion of Typical Parameter Ranges

A.1 Physical Interpretation of the Model

System (2)-(4) is well-known as traveling wave model describing longitudinal dynamical effects in semiconductor lasers [16], [23], [30]. Results of numerical computations have been presented in [3], [5], [6], [19], [30].
The travelling wave equations (2), (3) describe the complex optical field E in a spatially modulated waveguide:

$$E(\vec{r},t) = E(x,y) \cdot (\psi_1(t,z)e^{i\omega_0 t - \frac{\pi}{\Lambda}z} + \psi_2(t,z)e^{i\omega_0 t + \frac{\pi}{\Lambda}z}).$$

The complex amplitudes $\psi_{1,2}(t,z)$ are the longitudinally slowly varying envelopes of E. The transversal space directions are x and y, the longitudinal direction is z, and $\vec{r} = (x,y,z)$. For periodically modulated waveguides, Λ is longitudinal modulation wavelength. The central frequency is $\omega_0/(2\pi)$, and $E(x,y)$ is the dominant transversal mode of the waveguide.
The equations (2), (3) for an uncoupled waveguide ($\kappa = 0$) and a monochromatic light-wave in forward direction $e^{i\omega t}\psi_1(z)$ imply a spatial shape of the power $|\psi_1|^2$ according to

$$\partial_z |\psi_1(z)|^2 = (2\,\mathrm{Re}\,\beta(z) + 2\,\mathrm{Re}\,\chi(i\omega,z))|\psi_1(z)|^2 \tag{23}$$

where

$$\chi(i\omega,z) = \frac{\rho(z)\Gamma(z)}{i\omega - i\Omega_r(z) + \Gamma(z)}. \tag{24}$$

$2\,\mathrm{Re}\,\chi(i\omega,z))$ is a Lorentzian intended to fit the gain curve of the waveguide material (see Fig. 18). Hence, system (2), (3) produces gain dispersion, i. e., the spatial growth rate of the wave $e^{i\omega t}\psi(z)$ depends on its frequency ω. The variable $p(t,z)$ reports the internal state of the gain filter. See [21], [30] for more details. The Lorentzian gain filter is also used by [2], [16], [18]. Since the coefficients ρ, Γ and Ω are supposed to be spatially section-wise constant, $\chi(\lambda,z) = \chi_k(\lambda)$ for z in section S_k.
The equation (4) is a simple rate equation for the spatially averaged carrier density. It accounts for the current I, the spontaneous recombination $-n/\tau$, and the stimulated recombination.

A.2 Scaling of the Variables

In order to obtain the dimensionless quantities used in (2)-(4) and their possible ranges we have to scale the time t and the spatial variable z such that the coefficient

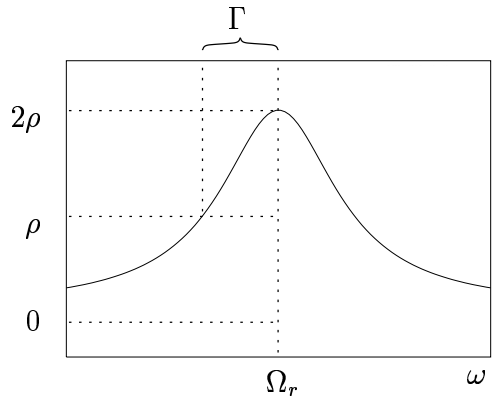

Figure 18: Shape of the Lorentzian $2\,\mathrm{Re}\,\chi(i\omega)$ *for* $\omega \in \mathbb{R}$ *and visualization of its parameters (see Table 2)*

	typical range	explanation
$\psi(t,z)$	$\mathbb{C}^2$	optical field, forward and backward travelling wave
$i \cdot p(t,z)$	$\mathbb{C}^2$	nonlinear polarization for the forward and backward travelling wave
$n(t)$	$(\underline{n}, \infty)$	spatially averaged carrier density in section S_1
$\mathrm{Im}\,\beta_k^0$	$\mathbb{R}$	frequency detuning
$\mathrm{Re}\,\beta_k^0$	< 0, $(-10, 0)$	internal losses
α_H	$(0, 10)$	negative of line-width enhancement factor
g_1	≈ 1	differential gain in S_1
κ_k	$(-10, 10)$	real coupling coefficients for the optical field ψ
ρ_k	$[0, 1)$	ρ_k is maximum of the gain curve
Γ_k	$O(10^2)$	half width of half maximum of the gain curve
$\Omega_{r,k}$	$O(10)$	resonance frequency
I	$O(10^{-2})$	current injection in section S_1
τ	$O(10^2)$	spontaneous lifetime for the carriers
P	$(0, \infty)$	scale of (ψ, p) (can be chosen arbitrarily)
r_0, r_L	$\mathbb{C}$, $\lvert r_0\rvert, \lvert r_L\rvert < 1$	facet reflectivities discontinuous in time

Table 2: Ranges and explanations of the variables and coefficients appearing in (2)-(7). *See also [30], [21] to inspect their relations to the originally used physical quantities and scales.*

in front of $\partial_z \psi$ is ∓ 1. Moreover, z is scaled such that $l_1 = 1$. The carrier density n in section S_1 is measured in multiples of the transparency carrier density (i. e. such that $G(1) = 0$). See table 2 for typical ranges of the quantities and [12] for further explanations.

References

[1] V. I. Arnold, V. S. Afrajmovich, Y. S. Ill'yashenko, L. P. Shil'nikov: *Bifurcation Theory.* In V. I. Arnold: Dynamical Systems V, Bifurcation and Catastrophe Theory. Springer Verlag, 1994.

[2] E. A. Avrutin, J. H. Marsh, J. M. Arnold: *Modelling of semiconductorlaser structures for passive harmonic mode locking at terahertz frequencies.* Int. J. of Optoelectronics vol. 10 No. 6 pp. 427-432, 1995.

[3] U. Bandelow: *Theorie longitudinaler Effekte in 1.55 μm Mehrsektions DFB-Laserdioden.* PhD-thesis, Humboldt-Universität Berlin, 1994.

[4] U.Bandelow, M. Radziunas, V. Tronciu, H.-J. Wünsche, F. Henneberger: *Tailoring the dynamics of diode lasers by dispersive reflectors.* Proceedings of SPIE, vol. 3944, pp. 536-545, 2000.

[5] U. Bandelow, L. Recke, B. Sandstede: *Frequency regions for forced locking of self-pulsating multi-section DFB lasers.* Optics Comm. 147, pp. 212-218, 1998.

[6] U. Bandelow, H.J. Wünsche, B. Sartorius, M. Möhrle: *Dispersive self Q-switching in DFB-lasers: Theory versus experiment.* IEEE J. Selected Topics in Quantum Electronics, Vol. 3, pp. 270-278, 1997.

[7] K. E. Brenan, S. L. Campbell, L. R. Petzold: *Numerical solution of initial-value problems in differential-algebraic equations.* North-Holland, New York, 1989

[8] E. J. Doedel, A. R. Champneys, T. F. Fairgrieve, Y. A. Kuznetsov, B. Sandstede, X. Wang: *AUTO97, Continuation and bifurcation software for ordinary differential equations.*

[9] J. L. A. Dubbeldam, B. Krauskopf: *Self-pulsation of lasers with saturable absorber: dynamics and bifurcations.* Opt. Comm. 159:325-338, 1999.

[10] K. Engelborghs: *DDE-BIFTOOL: a Matlab package for bifurcation analysis of delay differential equations.* Report TW305, Katholieke Universiteit Leuven, 2000.

[11] T. Erneux, F. Rogister, A. Gavrielides, V. Kovanis: *Bifurcation to mixed external cavity mode solutions for semiconductor lasers subject to external feedback.* Opt. Comm. 183:467-477, 2000.

[12] S. Friese: *Existenz und Stabilität von Lösungen eines Randanfangswertproblems der Halbleiterdynamik.* Thesis, Humboldt-Universität Berlin, 1999.

[13] E. M. Izhikevich: *Neural Excitability, Spiking and Bursting.* Int. J. of Bifurcation and Chaos, 10:1171-1266, 2000.

[14] R. Lang, K. Kobayashi: *External optical feedback effects on semiconductor injection properties.* IEEE J. of Quant. El., Vol. 16, pp. 347-355, 1980.

[15] Y. Kuznetsov: *Elements of Applied Bifurcation Theory.* Springer Verlag, 1995.

[16] D. Marcenac: *Fundamentals of laser modelling.* PhD thesis, University of Cambridge, 1993

[17] J. Mork, B. Tromborg, J. Mark: *Chaos in Semiconductor Lasers with Optical Feedback: Theory and Experiment.* IEEE J. of Quant. El., Vol. 28, No. 1, pp. 93-108, 1992.

[18] C. Z. Ning, R. A. Indik, J. V. Moloney: *Effective Bloch Equations for Semiconductor Lasers and Amplifiers.* IEEE J. of Quant. El., Vol. 33 No. 9, pp. 1543-1550, 1997.

[19] M. Radziunas, H.-J. Wünsche, B. Sartorius, O. Brox, D. Hoffmann, K. Schneider and D. Marcenac: *Modeling Self-Pulsating DFB Lasers with Integrated Phase Tuning Section.* to appear in IEEE J. of Quantum Electronics, 2000.

[20] J. Sieber: *Longitudinal Dynamics of Semiconductor Lasers.* PhD thesis, Humboldt-University of Berlin, 2001.

[21] J. Sieber, U. Bandelow, H. Wenzel, M. Wolfrum, H.-J. Wünsche: *Travelling wave equations for semiconductor lasers with gain dispersion.* WIAS Preprint No. 459, 1998.

[22] A. A. Tager, K. Petermann: *High-Frequency Oscillations and Self-Mode Locking in Short External-Cavity Laser Diodes.* IEEE J. of Quant. El. Vol. 30, No. 7, pp. 1553-1561, 1994.

[23] B.Tromborg, H. E. Lassen, H. Olesen: *Travelling Wave Analysis of Semiconductor Lasers.* IEEE J. of Quant. El. Vol. 30, No. 5 pp. 939-956, 1994.

[24] B. Tromborg, J. H. Osmundsen, H. Olesen: *Stability Analysis for a Semiconductor Laser in an External Cavity.* IEEE J. of Quant. El. Vol. 20, No. 9, pp. 1023–1032, 1984.

[25] V.Z. Tronciu, H.-J. Wünsche, J. Sieber, K. Schneider, F. Henneberger: *Dynamics of single mode semiconductor lasers with passive dispersive reflectors.* submitted to Optics Communcations, April 2000, accepted June.

[26] D. Turaev: *Fundamental obstacles to self-pulsations in low-intensity lasers.* WIAS Preprint 629, 2001.

[27] A. Vanderbauwhede, G. Iooss: *Center Manifold Theory in Infinite Dimensions.* Dynamics Reported Vol. 1(1992), pp 125-163, 1992.

[28] S. Wieczorek, B. Krauskopf, D. Lenstra: *A unifying view of bifurcations in a semiconductor laser subject to optical injection.* Opt. Comm. 172:279-295, 1999.

[29] H.J.Wünsche, O.Brox, M.Radziunas and F.Henneberger: *Excitability of a Semiconductor Laser by a Two-Mode Homoclinic Bifurcation.* submitted to PRL

[30] U. Bandelow, M. Wolfrum, J. Sieber, M. Radziunas: *Spatio-Temporal Dynamics of Multisection DFB-lasers with Gain Dispersion.* to appear in IEEE.

[31] H. Wenzel, U. Bandelow, H.-J. Wünsche, J. Rehberg: *Mechanisms of fast self pulsations in two-section DFB lasers.* IEEE J. Quantum Electron. Vol. 32, No. 1, pp. 69-79, 1996.